Journal of Materials Chemistry A

ROYAL SOCIETY OF CHEMISTRY

PAPER

View Article Online
View Journal | View Issue

Cite this: J. Mater. Chem. A, 2024, 12, 26064

The effects of $Yb_{11}Sb_{10}$ and $Yb_{10}MnSb_9$ secondary phases on the high performing thermoelectric material $Yb_{14}MnSb_{11}$†

Leah Borgsmiller and G. Jeffrey Snyder *

The $Yb_{11}Sb_{10}$ Zintl phase has long been reported to be a negative secondary phase in the high performing $Yb_{14}MSb_{11}$ (M = Mn, Mg, Zn) (14-1-11) thermoelectric material. However there have been discrepancies in the literature regarding the effect of this $Yb_{11}Sb_{10}$ phase on the thermoelectric performance of 14-1-11 compounds. The recent discovery of $Yb_{10}MnSb_9$ is used here to explain these inconsistencies. $Yb_{11}Sb_{10}$ and $Yb_{10}MnSb_9$ are very close materials stoichiometrically and crystallographically. However, despite these similarities, these materials exhibit very different transport properties and thus should have differing impacts on the overall thermoelectric performance of 14-1-11. In this work, we consider how these two phases affect the thermoelectric performance of $Yb_{14}MnSb_{11}$ when present as secondary phases both through an experimental investigation and an effective medium theory model. Secondary phases in thermoelectrics are often regarded as a consistently negative effect and yet here we show that while the presence of $Yb_{11}Sb_{10}$ in $Yb_{14}MnSb_{11}$ reduces the thermoelectric performance, the presence of $Yb_{10}MnSb_9$, even in large amounts does not dramatically reduce the thermoelectric performance and is shown here to even improve performance. This work provides a deeper understanding of previous works regarding 14-1-11 materials and Yb–Mn–Sb phases and paves the way towards practical application.

Received 3rd July 2024
Accepted 3rd September 2024

DOI: 10.1039/d4ta04606d

rsc.li/materials-a

Introduction

Thermoelectric materials that allow for the interconversion between heat and electricity,[1] are useful for a variety of different applications including distributed and localized cooling applications,[2] waste heat utilization,[3] and perhaps most important historically, powering space missions.[4] For these extraterrestrial applications such as providing electricity for the Mars rovers, the thermoelectric materials used must reach high values of efficiency at high operating temperatures.[4] The efficiency of a thermoelectric material in converting heat to electricity is dependent upon the thermoelectric figure of merit, zT. The zT of a material is given by the equation $zT = \frac{\alpha^2\sigma}{\kappa}T$, where α is the Seebeck coefficient, σ is the electrical conductivity, and κ is the total thermal conductivity.[1] The zT of any thermoelectric material will peak at an ideal operating temperature. Efforts to improve the zT of a material will often involve optimizing the charge carrier concentration, n, which has an impact on all of the terms in the equation for zT,[1] and trying to improve material properties independent of each other such as through introducing scattering sources to reduce the lattice thermal conductivity.[5,6] Phase boundary mapping[7] and grain boundary engineering[8] are two such strategies that have been utilized to improve thermoelectric performance.

While there are a handful of material systems to date that have exhibited zTs greater than 1 at these high operating temperatures,[9–12] making them candidates for practical applications, the search for new thermoelectric materials with promising properties is still on-going. The success of the high performing 14-1-11 Zintl thermoelectric compounds including $Yb_{14}MnSb_{11}$,[13] $Yb_{14}MgSb_{11}$,[14] and more recently $Yb_{14}ZnSb_{11}$,[9] has lead to other discoveries of Zintl thermoelectrics with similar compositions, namely $Yb_{21}Mn_4Sb_{18}$ [15] and $Yb_{10}MnSb_9$.[16] Zintl phases are defined as being valence precise where the electropositive cations donate electrons to polyanionic covalent structures.[17] Zintl phases are among some of the highest performing thermoelectric materials due to their often intrinsically low thermal conductivity from large complex unit cells and their semiconducting nature that together simultaneously allow for facile charge transport and impeded thermal transport.[18–20]

It can be seen that these Yb–Mn–Sb materials exist in a very busy region of phase space with multiple stable ternary and Yb–Sb binary compounds (Fig. 1), many of which can be described through Zintl–Klemm formalism. In particular, the $Yb_{11}Sb_{10}$ phase has been reported as an undesirable secondary phase that is often present, sometimes in large amounts, in 14-1-11 samples.[29] This secondary phase is expected to harm performance as it has been reported to be a fairly metallic phase with

Northwestern University, Department of Materials Science and Engineering, Evanston, IL 60208, USA. E-mail: jeff.snyder@northwestern.edu

† Electronic supplementary information (ESI) available. See DOI: https://doi.org/10.1039/d4ta04606d

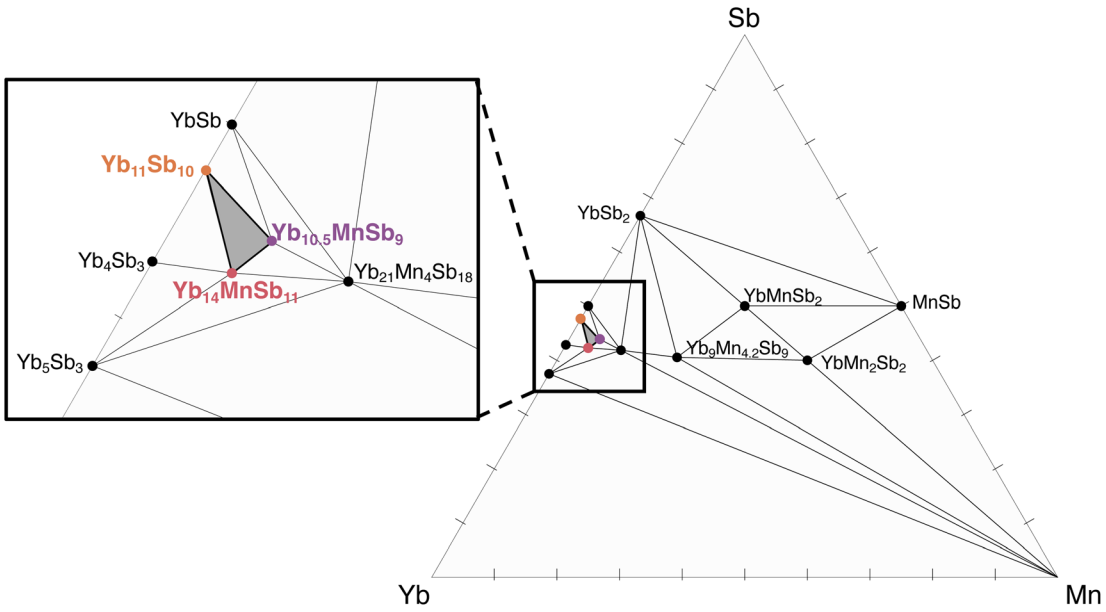

Fig. 1 Schematic phase diagram showing the reported phases in the Yb–Mn–Sb phase space. Many of these phases are reported in computational databases like the Materials Project[21] and OQMD,[22,23] while others are found from experimental reports.[13,15,16,24–27] The rectangle on the left is showing a zoomed-in region of the ternary diagram which is particularly busy around the high performing $Yb_{14}MnSb_{11}$ phase. The shaded three-phase region with $Yb_{14}MnSb_{11}$,[13] $Yb_{10.5}MnSb_9$,[16] and $Yb_{11}Sb_{10}$ [28] is the primary focus of this work.

a low Seebeck coefficient, high electrical conductivity, and high thermal conductivity.[30] However, many reports indicate that samples with 10% or more $Yb_{11}Sb_{10}$ have transport properties largely unaffected by this metallic phase.[29,31] This phase is also seemingly present, even when samples are made in Mn excess.[29] This would not be expected if the sample was synthesized in thermodynamic equilibrium in a Mn-rich phase space given what is understood about this ternary phase diagram shown in Fig. 1. Additionally, in one particularly contrarian example in the thesis of Hu (2017),[32] it was found that the presence of $Yb_{11}Sb_{10}$ in large amounts (~50%) in Bi-doped $Yb_{14}MgSb_{11}$ actually improved the thermoelectric properties through an increase in the Seebeck coefficient and a decrease in the thermal conductivity. This observation cannot be explained solely by this $Yb_{11}Sb_{10}$ phase. It would not be expected this phase with an incredibly low Seebeck coefficient would contribute to increasing the Seebeck coefficient in 14-1-11 samples.

However, we can reconcile these observations regarding $Yb_{11}Sb_{10}$ in 14-1-11 samples by considering the newly reported $Yb_{10}MSb_9$ material (M = Mn,[33] Mg[34]). While the $Yb_{11}Sb_{10}$ phase has been known for decades,[28] this $Yb_{10}MSb_9$ material was only first reported in 2021,[16] years after much of the foundational work regarding $Yb_{14}MSb_{11}$ (M = Mn, Mg, Zn). Due to the incredibly similar crystal structures between $Yb_{11}Sb_{10}$ and $Yb_{10}MSb_9$, it is likely that some amount of $Yb_{10}MSb_9$ could be misidentified as $Yb_{11}Sb_{10}$.[16]

While our previous work has considered the thermoelectric properties of this new 10-1-9 phase through transport measurements,[33,35] electronic structure evaluation,[36] and doping studies,[34] this work aims to tackle a different issue. Secondary phases have been frequently reported in these Yb–Mn–Sb Zintl phases and are difficult to control. Here we consider how the likely presence of this 10-1-9 phase impacts the thermoelectric performance of the $Yb_{14}MnSb_{11}$ material which has been of interest to the thermoelectric community for years.

In this work we will consider the implications of both $Yb_{11}Sb_{10}$ and $Yb_{10}MnSb_9$ as key secondary phases in $Yb_{14}MnSb_{11}$ through a combination of analytical and experimental approaches. To analyze the effect of these secondary phases, bulk polycrystalline $Yb_{14}MnSb_{11}$ samples were synthesized with purposeful addition of secondary phases $Yb_{11}Sb_{10}$ and $Yb_{10}MnSb_9$. The thermal and electronic transport of these samples as well as the X-ray diffraction (XRD) patterns were then compared to the pristine $Yb_{14}MnSb_{11}$ sample. Complementary computational techniques such as effective medium theory were then utilized to further explore the impacts of these phases on the thermoelectric performance of $Yb_{14}MnSb_{11}$. We show that while the presence of $Yb_{11}Sb_{10}$ alone is not sufficient to explain experimental trends with secondary phases in $Yb_{14}MnSb_{11}$, the additional consideration of $Yb_{10}MnSb_9$ as a secondary phase allows us to fully explain previously observed results. Additionally, the presence of $Yb_{10}MnSb_9$ in 14-1-11 samples is shown to even *improve* thermoelectric performance across certain temperature regimes.

Results and discussion

The most likely secondary phases in 14-1-11

A major challenge in synthesizing and studying $Yb_{14}MnSb_{11}$ is that it exists in the very dense region of Yb–Mn–Sb phase space with many crystallographically complex stable compounds. Based on the phase diagram schematic in Fig. 1, it can be seen

that slight off stoichiometries resulting from synthesis could result in $Yb_{14}MnSb_{11}$ being in thermodynamic equilibrium with a variety of potential secondary phases. In theory, this material has the potential to exist in five different three-phase regions, that include the secondary phases of $Yb_{11}Sb_{10}$, $Yb_{10}MnSb_9$, $Yb_{21}Mn_4Sb_{18}$, Yb_5Sb_3 and Yb_4Sb_3. While carefully designed synthesis can allow for quite phase pure samples,[37] reports of issues with secondary phases can be found throughout the literature. In general, $Yb_{11}Sb_{10}$ is the most frequently reported and considered secondary phase which has been reported in amounts up to 50%.[29,32] Large amounts of $Yb_{11}Sb_{10}$ would correspond to an overall sample that is deficient in both Mn and Yb.

In order to consider the most likely secondary phases, we must first consider the key sources of elemental loss in synthesis and subsequent characterization. While it is possible for various off stoichiometries and elemental loss to occur during synthesis of $Yb_{14}MnSb_{11}$ which is particularly likely for Mn,[29] the largest source of elemental loss both in synthesis and subsequent experimental measurements is expected to be oxidation of Yb. Yb oxidizes quite readily, particularly at high temperatures, and this is a major problem for this material. In a study on the oxidation of 14-1-11 compounds, it was shown that large amounts of Yb_2O_3 form upon heating in air, particularly on the surface of the material.[38] This results in a core material that is Yb-deficient and reportedly contains large amounts of the $Yb_{11}Sb_{10}$ phase.[38] While high temperature thermoelectric synthesis and subsequent high temperature transport measurements are generally conducted under argon or high vacuum environments, any trace amounts of oxygen result in some Yb oxidation which has been observed through a discoloration of sample surfaces after measurement, even under high vacuum.

If we consider a model sample that starts out with a perfect 14-1-11 stoichiometry and then oxidizes, we can consider the expected resultant secondary phases. If this perfect composition sample only loses Yb through the formation of Yb_2O_3, we would expect both $Yb_{11}Sb_{10}$ and $Yb_{10}MnSb_9$ to be present as secondary phases in thermodynamic equilibrium. The respective phase fractions of these secondary phases can be predicted using simple ternary lever rule type approach, where the total composition must equal the sums of the respective compositions and concentrations of the constituent phases. This analysis is shown in Fig. 2. Here we can see that as Yb is removed from the bulk of the sample through surface oxidation, the phase fraction of $Yb_{14}MnSb_{11}$ continuously decreases with a corresponding rise in the amounts of $Yb_{10}MnSb_9$ and $Yb_{11}Sb_{10}$. This path in the three phase region is much closer to the $Yb_{10}MnSb_9$ phase than the $Yb_{11}Sb_{10}$ phase which can be seen graphically in the top left inset of Fig. 2 which shows this three phase region of interest with an arrow along the line of decreasing Yb. This means that in cases where the dominant source of elemental off-stoichiometry is Yb loss, the most present secondary phase would be expected to be $Yb_{10}MnSb_9$. In order for there to be more $Yb_{11}Sb_{10}$ than $Yb_{10}MnSb_9$ in a 14-1-11 sample, there would have to be substantial loss of Mn as well. This is certainly possible, especially depending on the synthesis

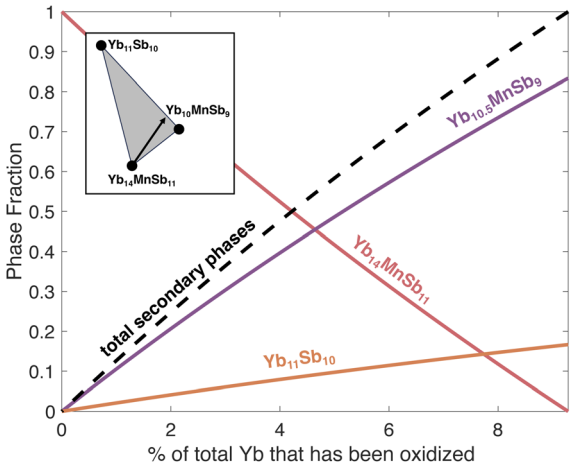

Fig. 2 Expected phase fractions (by moles) of $Yb_{14}MnSb_{11}$, $Yb_{10}MnSb_9$, and $Yb_{11}Sb_{10}$ as a result of Yb loss through oxidation calculated through a ternary lever rule method. As more Yb is lost, the phase fraction of $Yb_{14}MnSb_{11}$ decreases whereas the amount of $Yb_{10}MnSb_9$ and $Yb_{11}Sb_{10}$ increases. The dashed line depicts the total amount of $Yb_{10}MnSb_9$ and $Yb_{11}Sb_{10}$ secondary phases. The triangle in the top left corner depicts this three phase region of interest from the phase diagram in Fig. 1, with the arrow depicting the direction of Yb loss.

conditions. Mn makes up a very small percentage of 14-1-11 by atomic ratio, which is even smaller by mass. Given that the primary sources of elemental loss are considered to be Yb followed by Mn, it is likely that most 14-1-11 samples are in this three phase region between $Yb_{14}MnSb_{11}$, $Yb_{10}MnSb_9$, and $Yb_{11}Sb_{10}$.

Differentiation of secondary phases

In order to consider the thermoelectric implications for samples in this three-phase region, we must first consider the crystallography of these compounds. $Yb_{14}MnSb_{11}$ is a part of the greater 14-1-11 family of Zintl phases that have tetragonal unit cells comprised of Sb trimers, $MnSb_4$ tetrahedral units, and dispersed Yb cations for a total of 208 atoms per unit cell.[39] Similarly, $Yb_{11}Sb_{10}$ and $Yb_{10}MnSb_9$ also have large tetragonal unit cells with 84[28] and ~80–82[16,34,36] atoms per unit cell respectively. Note that the $Yb_{10}MnSb_9$ phase is better described by the stoichiometry $Yb_{10.5}MnSb_9$, which has been discussed previously[16,34] and is used throughout this work.

The key crystallographic similarities between $Yb_{11}Sb_{10}$ and $Yb_{10}MnSb_9$ are particularly apparent in the lattice parameters and the presence of Sb dimers amongst dispersed Yb cations. In the $Yb_{10}MnSb_9$ material there is also the presence of $MnSb_4$ tetrahedron, similar to those seen in $Yb_{14}MnSb_{11}$. These crystallographic similarities, along with general unit cell complexity, complicates secondary phase identification.

Generally, when synthesizing thermoelectric samples, XRD is an early step used to determine the presence of secondary phases in the material. However, the more complicated the unit cell, the more complicated the XRD patterns which makes differentiation between these phases, particularly as secondary phases, non-trivial.

In the original study identifying the $Yb_{10}MnSb_9$ phase, Baranets *et al.* warn that the similar crystal structures between $Yb_{10}MnSb_9$ and $Yb_{11}Sb_{10}$ could result in misidentification.[16] Further studies since then on the 10-1-9 structure have considered these structural similarities and differences.[35,40] These structural analyses have concluded that distinguishing between these two phases using XRD should use key differentiating peaks in the 26°–29° 2θ range (for Cu Kα radiation). These peaks are shown in Fig. 3 and are indicated by the diamond markers in the $Yb_{10}MnSb_9$ pattern.

However, while it is clear that we can use these peaks to differentiate between $Yb_{10}MnSb_9$ and $Yb_{11}Sb_{10}$, as has been done previously,[35] these marked peaks overlap with higher intensity peaks in $Yb_{14}MnSb_{11}$. Thus, while XRD patterns of 14-1-11 samples can tell us if a sample contains some amount of $Yb_{11}Sb_{10}$/$Yb_{10}MnSb_9$, it is incredibly difficult to determine if those secondary phases are $Yb_{11}Sb_{10}$, $Yb_{10}MnSb_9$ or a combination of the two using XRD alone. Looking back at previous reports of $Yb_{11}Sb_{10}$ in $Yb_{14}MnSb_{11}$, it is quite plausible that at least some of these samples contain $Yb_{10}MnSb_9$ in addition to or instead of $Yb_{11}Sb_{10}$. Since using XRD alone is not a straightforward way to differentiate between these materials in 14-1-11 samples, a further investigation of the transport properties is beneficial in our understanding of these materials as secondary phases.

In order to experimentally investigate the impacts of these phases on $Yb_{14}MnSb_{11}$, three different samples were synthesized from the same batch of $Yb_{14}MnSb_{11}$ ball-milled powder. One sample was comprised of only this stoichiometric 14-1-11 powder, while the other two were synthesized with 20% by weight of $Yb_{11}Sb_{10}$ and $Yb_{10}MnSb_9$ respectively (see the methods section for more detail). This 20% secondary phases by weight corresponds to 17% secondary phases by molar ratio. This purposeful addition of secondary phases is reminiscent of the phase boundary mapping approach.[7]

Here we should note, that while we have added powder made with stoichiometric $Yb_{11}Sb_{10}$ and $Yb_{10.5}MnSb_9$, to stoichiometric $Yb_{14}MnSb_{11}$, the complexity of the phase diagram and XRD patterns makes it difficult to confidently synthesize phase pure samples. If we consider the previous discussion on the problem with elemental loss, it perhaps might be likely that any of these three "pure" stoichiometries contains some amount of the other two phases as secondary phases. Here the goal is to consider how these secondary phases are expected to impact performance and utilize purposeful addition of secondary phases to probe this. We aim to point to the complexity of the problem and show general trends with changing stoichiometries of these samples. There is expected to be some margin of error however on the amount of secondary phases in these materials. For instance, while we added 20% by weight of powder synthesized in the stoichiometry 10.5-1-9 to powder synthesized with the stoichiometry 14-1-11, the final material might not have exactly 20% by weight of the $Yb_{10.5}MnSb_9$ phase. If the starting 14-1-11 material became slightly Yb-deficient during synthesis, it might already have some undetectable amounts of the 10.5-1-9 phase, meaning that the final sample in this case could have more than 20% secondary phases. However, regardless of precise amounts of secondary phases, we will see in the following analysis that these two phases are expected to impact thermal and electrical transport when present in 14-1-11.

The XRD patterns for these three synthesized samples are shown in Fig. 4. In general, all three samples have peak patterns that match well to the theoretical pattern for $Yb_{14}MnSb_{11}$ shown in black. We can then consider if XRD can indicate to us that these samples contain the expected secondary phases of $Yb_{11}Sb_{10}$ and $Yb_{10}MnSb_9$ respectively. As discussed previously and shown in Fig. 3, the best way to differentiate between $Yb_{10}MnSb_9$ and $Yb_{11}Sb_{10}$ is to consider lower intensity low angle peaks in the pattern which we do here in Fig. 4b. It is clear that the samples containing the added secondary phases exhibit additional short peaks around 2θ values of 25.7° and 27.6° (indicated by stars in Fig. 4b). However both the sample with added $Yb_{11}Sb_{10}$ and the sample with added $Yb_{10}MnSb_9$ exhibit

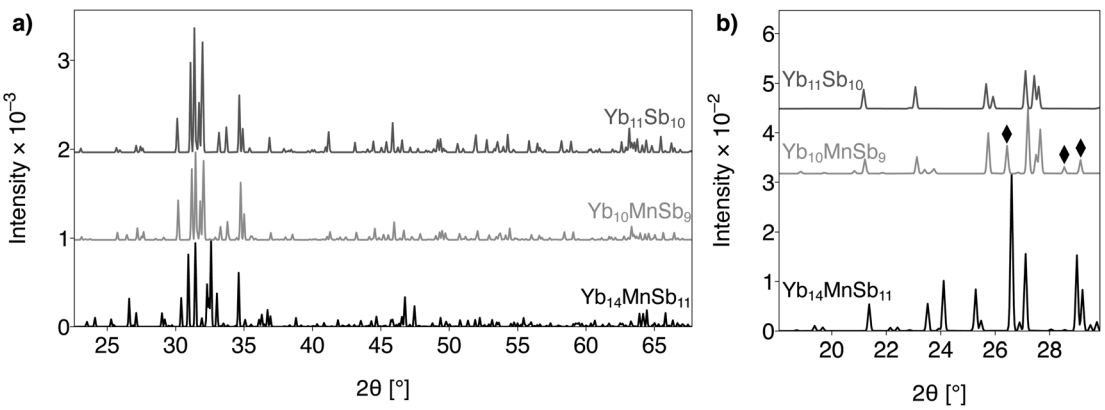

Fig. 3 Comparison of expected XRD patterns (from CIF files generated from literature single crystal data) for $Yb_{11}Sb_{10}$,[28] $Yb_{10}MnSb_9$,[16] and $Yb_{14}MnSb_{11}$ [39] with a Cu Kα radiation source in both a larger 2θ range (a), and a shorter 2θ range (b). While $Yb_{11}Sb_{10}$ and $Yb_{10}MnSb_9$ share most of the same peaks, there are a few key differentiating peaks at low angles which are present for $Yb_{10}MnSb_9$ but not $Yb_{11}Sb_{10}$ which are indicated by the black diamond-shaped markers.[16,40] However these indicated peaks overlap with higher intensity $Yb_{14}MnSb_{11}$ peaks, meaning that while we can differentiate between $Yb_{11}Sb_{10}$ and $Yb_{10}MnSb_9$, that task becomes more difficult when they are secondary phases in 14-1-11.

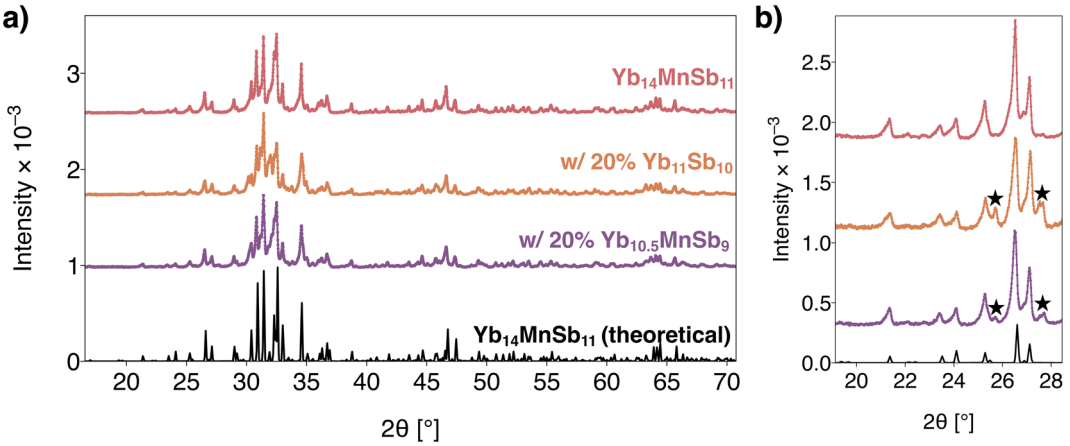

Fig. 4 (a) XRD patterns for the three experimental $Yb_{14}MnSb_{11}$ samples ($Yb_{14}MnSb_{11}$, $Yb_{14}MnSb_{11}$ with 20 wt% $Yb_{11}Sb_{10}$, and $Yb_{14}MnSb_{11}$ with 20 wt% $Yb_{10}MnSb_9$ respectively), and the theoretical pattern for $Yb_{14}MnSb_{11}$ shown in black. (b) Zoomed-in section of the XRD patterns, the black stars are indicative of both $Yb_{11}Sb_{10}$ and $Yb_{10}MnSb_9$. Here it can be seen that while the samples containing extra phases exhibit additional low angle peaks, the key distinguishing peaks from Fig. 3 are not readily observed due to the overlap with 14-1-11 peaks.

these additional peaks and thus it is difficult to visually detect differences between the two diffraction patterns. This can be attributed to the fact that the key peaks that are different between $Yb_{11}Sb_{10}$ and $Yb_{10}MnSb_9$ overlap with higher intensity 14-1-11 peaks as discussed with Fig. 3.

We then considered if Rietveld refinement[41] could be utilized to differentiate between these samples. Here it was found that for the samples with purposeful addition of secondary phases, the refinement was improved when the secondary phases of $Yb_{11}Sb_{10}$ and $Yb_{10}MnSb_9$ were included in the refinement. However, differences in the final R_w values were not significantly different if the refinement considered just $Yb_{11}Sb_{10}$ and $Yb_{14}MnSb_{11}$ *versus* just $Yb_{10}MnSb_9$ and $Yb_{14}MnSb_{11}$ for both samples. Thus, while Rietveld refinement and XRD as a whole are useful tools for determining if 14-1-11 samples have some $Yb_{10}MnSb_9/Yb_{11}Sb_{10}$ phases, it cannot concretely differentiate between these two secondary phases in small amounts, especially in these bulk polycrystalline samples of $Yb_{14}MnSb_{11}$. Additionally due to the nature of Rietveld refinement, it is always possible that in adding phases to the refinement, the improvements in fit are coming from the additional fitting parameters in a non-meaningful way. Perhaps higher resolution XRD on larger crystal samples could allow for better differentiation. However, much of the literature on 14-1-11 materials for thermoelectric applications use similar polycrystalline synthesis and XRD methods. Other common methods of secondary phase identification such as electron microscopy (SEM) and energy dispersive spectroscopy (EDS) that rely on compositional contrast are also difficult for this system due to the incredibly similar stoichiometries and thus minimal compositional contrast between phases.

Effects of secondary phases on thermoelectric transport

Despite the obstacles with phase identification, since $Yb_{11}Sb_{10}$ and $Yb_{10}MnSb_9$ exhibit very different electronic and thermal properties, one would expect that they would have different effects on the transport of $Yb_{14}MnSb_{11}$ when present in substantial amounts as secondary phases. While $Yb_{10}MnSb_9$ has been shown to be a decent thermoelectric with a moderate zT,[7,34] $Yb_{11}Sb_{10}$ is a poor metal with a very low zT.[30] Experimentally measured thermal and electrical transport of $Yb_{14}MnSb_{11}$, $Yb_{11}Sb_{10}$, and $Yb_{10}MnSb_9$ are shown in Fig. 5. Here it can be seen that $Yb_{10}MnSb_9$ and $Yb_{11}Sb_{10}$ exhibit very different

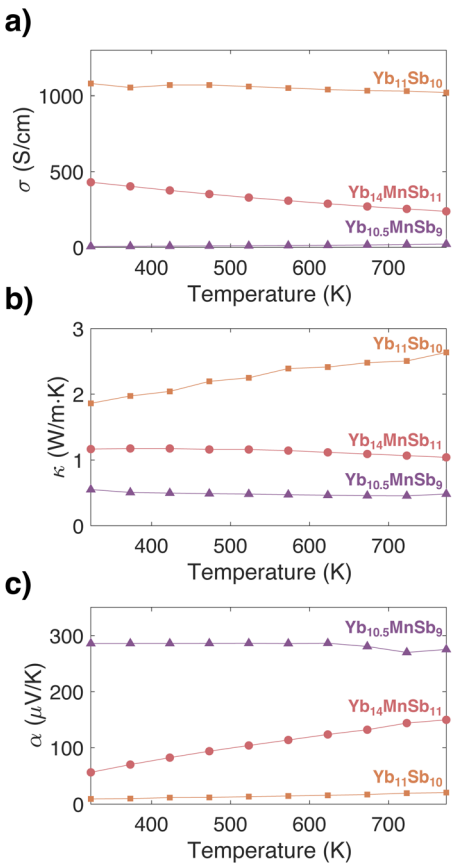

Fig. 5 Transport properties for single phase $Yb_{14}MnSb_{11}$, $Yb_{11}Sb_{10}$ and $Yb_{10}MnSb_9$ (a) electrical conductivity, σ, (b) total thermal conductivity, κ, and (c) Seebeck coefficient, α.

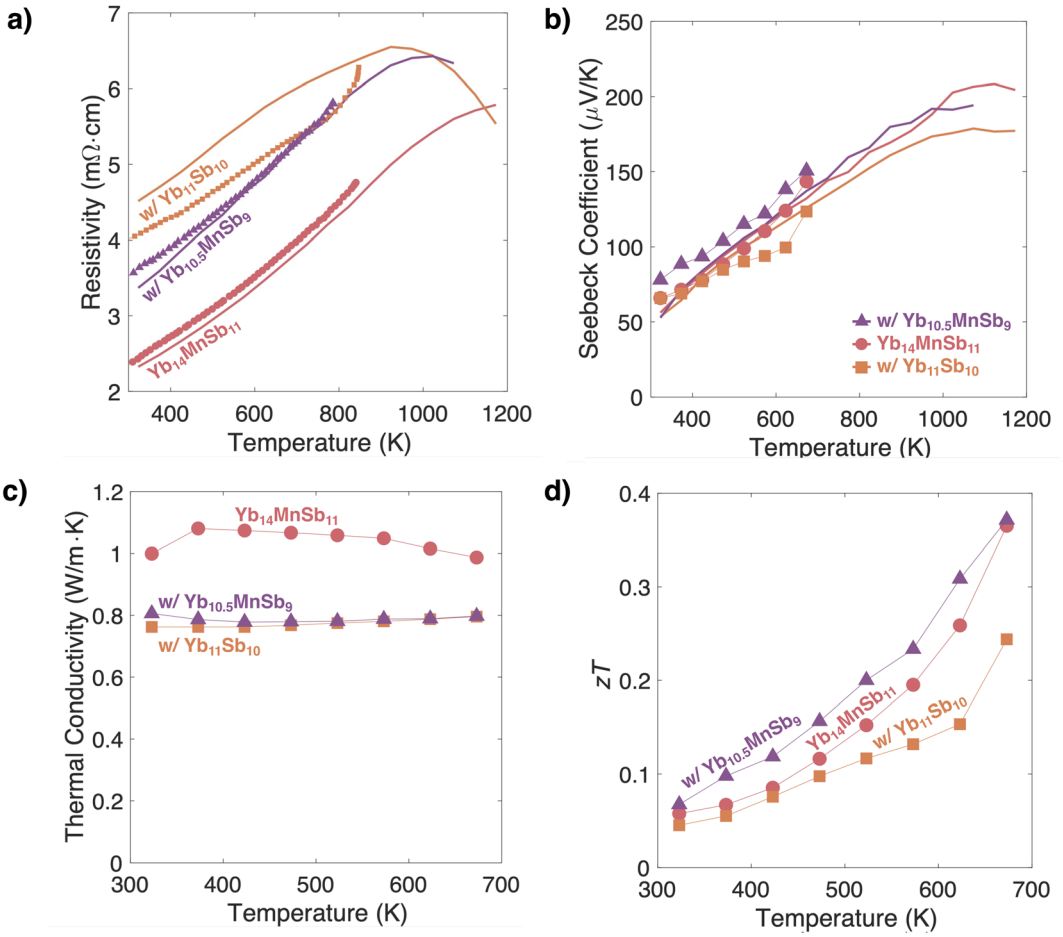

Fig. 6 Transport for various samples of $Yb_{14}MnSb_{11}$ including phase pure samples, and samples with 20% by weight $Yb_{11}Sb_{10}$ and $Yb_{10}MnSb_9$ respectively (corresponding to 17% by moles). The shown transport includes the (a) electrical resistivity (b) Seebeck coefficient (c) thermal conductivity and (d) zT. The solid lines in (a) and (b) correspond to higher temperature data obtained with a different set of samples synthesized with the same process and measured at NASA's Jet Propulsion Laboratory (JPL) which show decent agreement with overall trends.

transport, with the properties of $Yb_{14}MnSb_{11}$ intermediary between the two. Thus if we consider the Seebeck coefficient for example, we would expect large amounts of $Yb_{10}MnSb_9$ in $Yb_{14}MnSb_{11}$ to increase the Seebeck coefficient, whereas large amounts of $Yb_{11}Sb_{10}$ in $Yb_{14}MnSb_{11}$ should decrease the Seebeck coefficient.

The expected and observed effects of these secondary phases on transport can be considering through a dual approach utilizing both experimental data (Fig. 6) and effective medium theory (Fig. 7).

Experimental transport trends. Plots of the electrical resistivity, Seebeck coefficient, thermal conductivity and zT for these samples are shown in Fig. 6. The solid lines in Fig. 6a and b, correspond to a second set of samples with identical synthesis that were measured up to higher temperatures at NASA's Jet Propulsion Laboratory (JPL). There is good agreement in the overall trends of these two sets of samples with identical synthesis but slightly different measurement apparatuses. Considering first the electrical resistivity in Fig. 6a, it can be seen that both samples containing additional $Yb_{11}Sb_{10}$ and $Yb_{10}MnSb_9$ show an increased resistivity with respect to the pure compound. This resistivity increase is greater for samples with added $Yb_{11}Sb_{10}$ than for those with added $Yb_{10}MnSb_9$. This generally agrees with previous studies, where more resistive samples were attributed to the greater presence of secondary phases.[29,32]

We can next consider the impact of secondary phases on the Seebeck coefficient. Here in Fig. 6b, it can be seen that the presence of $Yb_{10}MnSb_9$ slightly increases the Seebeck coefficient (until very high temperatures where $Yb_{10}MnSb_9$ exhibits bipolar conduction before $Yb_{14}MnSb_{11}$). Conversely, the presence of $Yb_{11}Sb_{10}$ reduces the Seebeck coefficient as one might expect from the addition of a more metallic phase. We can consider the Seebeck coefficient to be a direct reflection of the carrier concentration of a material due to the relationship between α and Fermi level. Thus, we would expect a more metallic sample with a lower Seebeck coefficient (the one with additional $Yb_{11}Sb_{10}$) to have a higher carrier concentration, whereas a more insulating sample with a higher Seebeck coefficient should have a lower carrier concentration (the sample with the additional $Yb_{10}MnSb_9$). However, the differences in Seebeck coefficient and thus overall carrier concentration

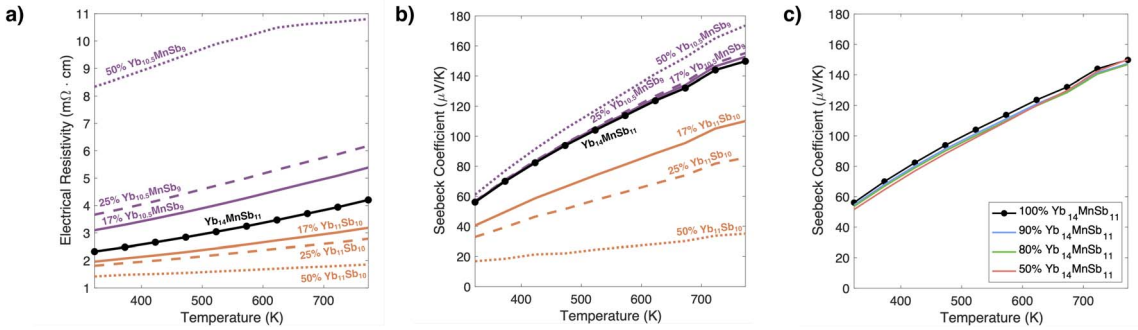

Fig. 7 Effective medium theory predictions of transport for $Yb_{14}MnSb_{11}$ samples containing some amount of $Yb_{10}MnSb_9$ and/or $Yb_{11}Sb_{10}$. In each plot the black line corresponds to experimental data for phase pure $Yb_{14}MnSb_{11}$ (a) the predicted effective electrical resistivity for samples of $Yb_{14}MnSb_{11}$ containing 17%, 25%, and 50% (mole%) of $Yb_{10}MnSb_9$ and $Yb_{11}Sb_{10}$ respectively. Note that this does not match experimental trends for the sample containing $Yb_{11}Sb_{10}$, pointing to the possibility of interfacial effects. (b) The predicted effective Seebeck coefficients for samples of $Yb_{14}MnSb_{11}$ containing 17%, 25%, and 50% (mole%) of $Yb_{10}MnSb_9$ and $Yb_{11}Sb_{10}$ respectively. (c) Predicted Seebeck coefficient curves for samples that are Yb deficient and have secondary phase fractions as predicted from Fig. 2. Here samples that range between 100% $Yb_{14}MnSb_{11}$ and 50% $Yb_{14}MnSb_{11}$ have very minimal differences in the Seebeck curve.

between the samples synthesized here are relatively small, due to the fact that these samples with additional secondary phases are still primarily 14-1-11 which has a relatively high undoped carrier concentration. Hall effect measurements of the samples measured at NASA JPL are provided in the ESI, Fig. S1.† All samples have a carrier concentration around 1×10^{21} cm^{-3} with the noise in the measurement greater than the differences between samples.

Note that in this work no dopants are used because $Yb_{14}MSb_{11}$ (M = Mn, Mg, Zn) achieves a maximum $zT > 1$ without the use of any dopants. This occurs because the compound has a valence imbalance leading to 1 hole per formula unit. The other semiconducting phase, 10-1-9 is also intrinsically doped, meaning that there are intrinsic defects, typically cation vacancies, that lead to excess holes. The three phase equilibrium between 14-1-11, 11-10 and 10-1-9 ensures that the intrinsic defect concentration is the same for any compositional mixture of the three phases.[7]

In this study we also report the trends in total thermal conductivity (Fig. 6c) and zT (Fig. 6d) with temperature and these secondary phases. It can be seen that the presence of either secondary phase reduces the thermal conductivity as expected from the corresponding increase in electrical resistivity. Calculating the zT using the measured transport data, shows that the presence of $Yb_{10}MnSb_9$ increases the zT slightly across this temperature range, whereas the presence of $Yb_{11}Sb_{10}$ decreases the zT slightly. However it should be noted that at higher temperatures where $Yb_{14}MnSb_{11}$ is of most interest, we would expect the zT of pure $Yb_{14}MnSb_{11}$ to be greater than that of $Yb_{14}MnSb_{11}$ with $Yb_{10}MnSb_9$ due to the earlier bend over in the Seebeck coefficient with $Yb_{10}MnSb_9$.

Effective medium theory model. Effective medium theory models allow for the calculation of effective or overall bulk properties as a result of contributions from multiple components within a material and has been used in various studies on thermoelectric materials.[42–45] Effective medium theory can be used to consider a variety of transport properties including the electrical conductivity[46,47] and Seebeck coefficient.[48–50]

A commonly used formulation of the electrical conductivity using effective medium theory is as follows:[46]

$$\sum_i \chi_i \frac{\sigma_i - \sigma_{\text{eff}}}{\sigma_i + 2\sigma_{\text{eff}}} = 0 \quad (1)$$

Here, χ_i represents the phase fraction of the specific phase with electrical conductivity, σ_i and the σ_{eff} term is the overall effective conductivity of the sample. This equation has been applied to two phase samples of $Yb_{11}Sb_{10}$, and $Yb_{10}MnSb_9$, where the theory matched experimental observations well.[35]

We can use this equation to consider what trends we might expect in the resistivity $\left(\rho = \frac{1}{\sigma}\right)$ when $Yb_{11}Sb_{10}$ and $Yb_{10}MnSb_9$ are present in $Yb_{14}MnSb_{11}$. This is shown in Fig. 7a, where there is experimental data for $Yb_{14}MnSb_{11}$, and then predicted effective medium theory resistivities for $Yb_{14}MnSb_{11}$ with 50% (mole percent) $Yb_{10}MnSb_9$, 25% $Yb_{10}MnSb_9$, 17% $Yb_{10}MnSb_9$, 17% $Yb_{11}Sb_{10}$, 20% $Yb_{11}Sb_{10}$, and 50% $Yb_{11}Sb_{10}$. Because $Yb_{11}Sb_{10}$ is metallic with a very low electrical resistivity (see Fig. 5), we would expect the presence of $Yb_{11}Sb_{10}$ to decrease the resistivity in $Yb_{14}MnSb_{11}$. Conversely, $Yb_{10}MnSb_9$ is much more electrical resistive and would be expected to increase the resistivity of $Yb_{14}MnSb_{11}$. However in comparing this result to the experimental result of Fig. 6 it can be seen that it was observed that both the presence of $Yb_{11}Sb_{10}$ and $Yb_{10}MnSb_9$ increased the overall sample resistivity. Thus while this formulation for effective medium theory conductivity held well for $Yb_{11}Sb_{10}$–$Yb_{10}MnSb_9$ composites,[35] this doesn't hold for these samples. This could be due to a number of reasons. To start, this effective medium theory formulation is quite simple and assumes spherical and isotropic phases. It also assumes that there is no effect from the interfaces between phases. In real materials, we know that grain boundaries can have significant impact on transport, which could be occurring here. Additionally, these samples were synthesized by hotpressing powders of

$Yb_{14}MnSb_{11}$ and crushed secondary phases pellets which could further exacerbate this interfacial effect. Thus, here using the dual approach of effective medium theory and experimental results, we can conclude that there are likely interfacial effects that are impacting the electrical resistivity. While uncovering the exact role of these interfaces would be difficult experimentally due to differing synthesis routes and difficulties in imaging the microstructure of these materials, we believe this would be a fascinating area of potential future work.

As was done with the electrical resistivity, we can consider the expected impact on the Seebeck coefficient through an effective medium theory approach. While the electrical conductivity can be largely affected by grain boundaries and interfacial effects, the Seebeck coefficient is expected to be relatively unaffected. We can use the following expression,[49] where χ_i is the phase fraction of the specific phase, i, σ_i is the electrical conductivity of the phase, and α_i is the Seebeck coefficient of the phase. The terms σ_{eff} and α_{eff} represent the overall expected effective values.

$$\sum_i \chi_i \frac{\sigma_i/\alpha_i - \sigma_{\text{eff}}/\alpha_{\text{eff}}}{\sigma_i/\alpha_i + 2\sigma_{\text{eff}}/\alpha_{\text{eff}}} \simeq 0 \quad (2)$$

In this work we utilize this expression because it can be more easily extended to a three-phase system unlike other expressions that are only considered for the simplest two-phase system.[48] Once again, this simple formulation of effective medium theory assumes that all secondary phase regions can be approximated to be spherical and isotropic. This formulation has been also shown to be most accurate for systems involving degenerate semiconductors and metals.[49] Additionally, it should be noted that this equation requires inputs of not only the Seebeck coefficients for the constituent phases but also the electrical conductivities of constituent phases and the overall effective conductivity. Here we utilize the effective conductivity equation (eqn (1)), although we have already shown that while this seems to describe the effect of $Yb_{10}MnSb_9$ well, it doesn't well describe the effect of $Yb_{11}Sb_{10}$, perhaps due to additional electrical interface resistance between $Yb_{14}MnSb_{11}$ and $Yb_{11}Sb_{10}$. Thus while the overall trends (increasing/decreasing) can be considered *via* this simple model, the predicted values may not be as accurate, particularly for the case of $Yb_{11}Sb_{10}$.

Considering now the predicted Seebeck curves in Fig. 7b, we can see that the Seebeck is expected to increase with the addition of $Yb_{10}MnSb_9$ and decrease with the addition of $Yb_{11}Sb_{10}$ which qualitatively agrees well with experimental results in Fig. 6b. It should also be noted that while the sample labeled $Yb_{14}MnSb_{11}$ was synthesized using a pure stoichiometric ratio without any purposeful addition of secondary phases, based on this analysis we believe it is plausible if not likely that there are still trace amounts of secondary phases formed such as through Yb loss from oxidation. If this were the case, there could be additional $Yb_{10}MnSb_9$ in all three samples beyond what was purposefully added, meaning that we might expect there to experimentally be a larger increase in Seebeck for the sample with added $Yb_{10}MnSb_9$ and a smaller decrease in Seebeck for the sample with added $Yb_{11}Sb_{10}$ which is seen here.

We can also use the phase fraction curves in Fig. 2 to model the expected Seebeck coefficients upon Yb loss through oxidation which is modeled in Fig. 7c. Here we show the experimental Seebeck curve for $Yb_{14}MnSb_{11}$, as well as curves for modeled samples with 90%, 80%, and 50% $Yb_{14}MnSb_{11}$, with the remaining 10–50% secondary phases that are a combination of $Yb_{10}MnSb_9$ and $Yb_{11}Sb_{10}$ as predicted from Fig. 2.

Here it can be seen that three-phase samples with 0–50% secondary phases, exhibit very little differences in the overall Seebeck curve. These differences are on the order of magnitude of potential error you might expect from a Seebeck experimental measurement. In contrast to the results in Fig. 7b which show that samples with 50% $Yb_{10}MnSb_9$ should demonstrate a more significant increase in Seebeck coefficient, and samples with 50% $Yb_{11}Sb_{10}$ should demonstrate an even more dramatic decrease in Seebeck coefficient, samples with 50% secondary phases containing a mixture of $Yb_{10}MnSb_9$ and $Yb_{11}Sb_{10}$ only change the overall Seebeck coefficient slightly.

Implications of these results for 14-1-11 data

These findings from experiment and effective medium theory can help explain experimental data from previous studies. For example, in the work of Grebenkemper *et al.*,[29] they show Seebeck curves for a variety of $Yb_{14}MnSb_{11}$ samples (some containing excess Mn) with reported amounts of $Yb_{11}Sb_{10}$ ranging from 0–39%. Despite the claim that some of these samples contain large amounts of the metallic $Yb_{11}Sb_{10}$ phase, the Seebeck curves are relatively the same for all samples. While we would expect large amounts of $Yb_{11}Sb_{10}$ without any $Yb_{10}MnSb_9$ in $Yb_{14}MnSb_{11}$ to drastically reduce the Seebeck coefficient (Fig. 7b), if these samples instead had a mixture of $Yb_{10}MnSb_9$ and $Yb_{11}Sb_{10}$, the Seebeck coefficient should remain relatively constant even with large amounts of impurity as suggested by the model in Fig. 7c. Since $Yb_{11}Sb_{10}$ and $Yb_{10}MnSb_9$ have essentially identical effects on the XRD pattern of $Yb_{14}MnSb_{11}$ and since $Yb_{10}MnSb_9$ was previously unreported at the time of this study, we can conclude that some portion of the reported "$Yb_{11}Sb_{10}$" phase is $Yb_{10}MnSb_9$ instead. Because of this report of the effect of large amounts of "$Yb_{11}Sb_{10}$", it was concluded in this study and others that the effect of $Yb_{11}Sb_{10}$ is minimal on these materials.[29,31] While it is true that there is a minimal effect of these secondary phases on the Seebeck coefficient and transport, this is likely due to the coexistence of both $Yb_{10}MnSb_9$ and $Yb_{11}Sb_{10}$ with expected opposite effects on transport. Additionally they report that as these samples are cycled through high temperature measurements this amount of secondary phase continues to increase. This can easily be explained by the oxidation of Yb resulting in larger fractions of these Yb-deficient secondary phases as modeled in Fig. 2. If the main elemental loss was Mn instead of Yb, we would expect the formation of substantial Yb_4Sb_3 in addition to $Yb_{11}Sb_{10}$ which is not reported.

If we consider a different study in the thesis of Hu (2017),[32] it was reported that samples of Bi-doped $Yb_{14}MgSb_{11}$ with 50% of

"$Yb_{11}Sb_{10}$" exhibited the highest zT, due to an increase in the Seebeck coefficient, increase in the electrical resistivity and decrease in the thermal conductivity compared to samples with less (but still present) secondary phases. This trend cannot be explained by the presence of $Yb_{11}Sb_{10}$, however it falls perfectly in alignment with what would be expected for a sample with substantial 10-1-9 phase that has been misidentified as $Yb_{11}Sb_{10}$. Note that in this study they were considering the Mg-analog of 14-1-11, $Yb_{14}MgSb_{11}$. However both $Yb_{14}MnSb_{11}$ and $Yb_{14}MgSb_{11}$ have incredibly similar transport[9] and so do $Yb_{10}MnSb_9$ and $Yb_{10}MgSb_9$.[34] Thus we would expect the trends of 10-1-9 in 14-1-11 to be roughly the same for the Mg case as is studied here for the Mn case. In consideration of this study, we show that the presence of $Yb_{10}MgSb_9$ as a secondary phase can explain previously contradictory results.

In addition to using this analysis to explain past results, we can use these results to predict the potential evolution of performance of a sample with time. A key consideration in designing thermoelectrics for practical applications is the stability of the material and how it evolves on timescales of utilization. In the case of $Yb_{14}MnSb_{11}$, the key evolution we might expect with time would be oxidation, with higher oxidation rates expected under conditions with higher oxygen environments and higher temperatures. If Yb from the sample is loss through oxidation, we would expect the breakdown of constituent phases to follow the trend discussed previously in Fig. 2. This means that with time we would expect the sample to continually decrease the amount of $Yb_{14}MnSb_{11}$ while substantially increasing the amount of $Yb_{10}MnSb_9$ and slightly increasing the amount of $Yb_{11}Sb_{10}$. This would correspondingly result in an observed shift in the XRD patterns indicating large amounts of these secondary phases. However, as we've shown here, $Yb_{10}MnSb_9$ is not expected to substantially harm the thermoelectric performance as we would expect $Yb_{11}Sb_{10}$ to do, and it has the potential to even improve performance. Thus, despite expected and observed changes in the phase purity with cycling, the thermoelectric performance is not expected to be dramatically harmed and thus this evolution is not as important of an issue as previously suspected for long term performance.

Conclusion

In this work we considered the impact of $Yb_{11}Sb_{10}$ and $Yb_{10}MnSb_9$ as the expected primary secondary phases in $Yb_{14}MnSb_{11}$ through an analysis of the phase diagram and XRD patterns, experimental synthesis and transport, as well as effective medium theory calculations. Since Yb loss through oxidation is expected to be the primary source of elemental loss, we expect $Yb_{10}MnSb_9$ to be the dominant secondary phase followed by $Yb_{11}Sb_{10}$. Since the XRD patterns of these two materials are virtually indistinguishable in $Yb_{14}MnSb_{11}$, it very likely that some amount of secondary phase previously identified in the literature as $Yb_{11}Sb_{10}$ was actually $Yb_{10}MnSb_9$. In general large amounts of $Yb_{10}MnSb_9$ are expected to increase the Seebeck coefficient of $Yb_{14}MnSb_{11}$, whereas $Yb_{11}Sb_{10}$ is metallic and expected to decrease the Seebeck coefficient, which we showed here both through experiment and effective medium theory calculations. However, both $Yb_{10}MnSb_9$ and $Yb_{11}Sb_{10}$ are found experimentally to increase the electrical resistivity. The origins of the increase in electrical resistivity from the addition of $Yb_{11}Sb_{10}$ is not expected from a simple effective medium theory approach and thus features like the microstructure could be considered in future work to understand this effect. In the room temperature to mid temperature regime, the presence of $Yb_{10}MnSb_9$ actually improves the overall thermoelectric performance. This is significant in that generally we consider the effects of secondary phases on these materials to be only negative. But here we can see that the presence of the $Yb_{10}MnSb_9$, can allow the material to have a somewhat constant if not greater zT. Additionally, here we show that the expected phase fractions of secondary phases resulting from loss of Yb such as through oxidation, give Seebeck coefficient curves that are relatively constant, even with secondary phases on the order of 50%. This allows us to explain previous studies where large amounts of seemingly $Yb_{11}Sb_{10}$ have relatively no effect on the thermopower. The presence of $Yb_{11}Sb_{10}$ alone as a secondary phase would not explain this trend. This work also allows us to consider the changes a sample may experience through oxidation, and despite the changing secondary phase fractions with oxidation, the performance is expected to be relatively unhindered allowing 14-1-11 materials to be viable options for long-term space applications. While 14-1-11 has been studied as a thermoelectric material for years, it is still yet to be utilized in practical applications in part due to issues with secondary phase formation. This work allows us to understand and anticipate the impacts of these secondary phases on performance and indicates that while $Yb_{10}MnSb_9$ is likely to be present, it will not change the fact that $Yb_{14}MnSb_{11}$ is an excellent thermoelectric material worthy of use in high temperature applications.

Methods

Sample synthesis

Bulk polycrystalline pellet samples were synthesized using a high energy ball milling and hot pressing approach. All of these samples contain Yb that was shaved from a bulk piece using a steel rasp in an argon glovebox, Mn that was purified by heating in a quartz tube to 1000 °C to remove surface oxide, and Sb shot (99.999%, 5N Plus).

First the Mn was pre-reacted with Sb forming a binary precursor MnSb as has been done in other 14-1-11 studies to mitigate the formation of undesirable Yb–Sb binaries.[29,37] This was done by combining Mn and Sb in a 1 : 1 molar ratio and sealing in a quartz tube under vacuum. This tube was then heated to 950 °C in a furnace at a rate of 100 °C per hour and held at temperature for 2 hours. Then the temperature was decreased to 675 °C and held there for 48 hours before an air quench by removing the tube from the furnace. The complete reaction was confirmed using powder XRD on a STOE STADI P instrument using Cu Kα radiation.

In order to synthesize the $Yb_{11}Sb_{10}$ and $Yb_{10.5}MnSb_9$ samples, the Yb, Sb and MnSb (in the case of $Yb_{10}MnSb_9$) were measured in their respective atomic ratios totalling 7 grams

each. These components were loaded into a stainless steel ball mill jar containing stainless steel balls in an argon glovebox and sealed with an O-ring. These mixtures were then mechanically alloyed through high energy ball-milling in a SPEX high energy ball mill. This was done for three 90 minute intervals, with the sides of the jar being scraped with steel tools in between each cycle to aid in the reaction.

This ball-milled powder was then hot-pressed into individual 1/2 inch diameter pellets using a home-built induction hot press[51] and graphite dies with graphoil and graphite spacers. These samples were pressed using ~2.3 g of powder each and pressed at 800 °C for 45 min at an average pressure ~45 MPa. XRD data for these as synthesized stoichiometric $Yb_{11}Sb_{10}$ and $Yb_{10.5}MnSb_9$ pellets are supplied in the ESI, Fig. S2.†

For the 14-1-11 samples, a single batch of powder with a synthesis composition of $Yb_{14}MnSb_{11}$ was made by combining Yb, MnSb, and Sb and ball-milling as described for the samples above totalling 10 grams. From this single batch of powder, three different samples were synthesized. The first sample contained only this $Yb_{14}MnSb_{11}$ powder totalling approximately 2.5 g. The second sample contained 2 g of this $Yb_{14}MnSb_{11}$ powder and 0.5 g of crushed $Yb_{11}Sb_{10}$ pellet (20% by weight) that was crushed using a mortar and pestle. Similarly, the last sample contained 2 g of $Yb_{14}MnSb_{11}$ and 0.5 g of crushed $Yb_{10.5}MnSb_9$ pellet. All three pellets were then hotpressed using the same methods as discussed for the previous series of samples. A second set of identical samples were then made and used for the XRD and high temperature transport measurements conducted at NASA Jet Propulsion Laboratory (JPL).

Measurements

Electrical transport measurements were conducted using home-built instruments. The temperature dependent electrical resistivity/conductivity was measured using the van der Pauw method with a four-point resistance probe in a home-built Hall effect instrument.[52] The Seebeck coefficients were measured using a home-built two point probe instrument with Nb-chromel thermocouples.[53] Both sets of measurements were conducted under dynamic vacuum up to 600 °C.

Higher temperature electrical transport measurements as shown by the solid lines in Fig. 6a and b, were measured at the NASA Jet Propulsion Laboratory using similar instruments up to 1000 °C.

Thermal transport was considered by measuring the thermal diffusivity using a Netzsch LFA 457 *MicroFlash* instrument. This measured thermal diffusivity was then converted to a thermal conductivity using the Dulong–Petit heat capacity and sample density measured using the Archemides method in isopropyl alcohol.

The electrical resistivity and thermal conductivity measurements done here (indicated by the markers in Fig. 6a and c) were measured and reported for heating curves. The Seebeck measurements done here (markers in Fig. 6b) as well as the Seebeck and resistivity curves measured at JPL (solid lines in Fig. 6a and b) were conducted in both heating and cooling conditions and the data points shown here are *averages* between the two curves rather than explicitly measured data points. The full data set is supplied in the ESI.† While there was some hysteresis, it was considered to be minimal and does not change the conclusions of this work.

X-ray diffraction measurements were conducted on bulk polycrystalline pellets in reflection mode on a STOE STADI MP instrument using Cu Kα radiation. Rietveld refinement was conducted using the GSAS-II software.[54]

Data availability

The data supporting this article have been included as part of the ESI.†

Conflicts of interest

The authors have no conflict to declare.

Acknowledgements

L. B. is supported by the National Science Foundation Graduate Research Fellowship Program under Grant No. DGE-1842165. Any opinions, findings, and conclusions or recommendations expressed in this material are those of the author and do not necessarily reflect the views of the National Science Foundation. We acknowledge the support from U.S. Department of Commerce, National Institute of Standards and Technology as part of the Center for Hierarchical Materials Design (CHiMaD) under Award No. 70NANB19H005. This material based upon work supported by the U.S. Department of Energy's Office of Energy Efficiency and Renewable Energy (EERE) under the Advanced Manufacturing Office (AMO) Award Number DE-EE0009104. This work made use of the IMSERC Crystallography facility at Northwestern University, which has received support from the Soft and Hybrid Nanotechnology Experimental (SHyNE) Resource (NSF ECCS-2025633), and Northwestern University. The authors would also like to acknowledge and thank Dr Kurt Star for assistance measuring some of these samples to high temperatures at NASA JPL.

References

1 G. J. Snyder and E. S. Toberer, Complex thermoelectric materials, *Nat. Mater.*, 2008, **7**, 105–114, DOI: **10.1038/nmat2090**.
2 G. J. Snyder, *et al.*, Distributed and localized cooling with thermoelectrics, *Joule*, 2021, **5**, 748–751, DOI: **10.1016/j.joule.2021.02.011**.
3 L. E. Bell, Cooling, heating, generating power, and recovering waste heat with thermoelectric systems, *Science*, 2008, **321**, 1457–1461, DOI: **10.1126/science.1158899**.
4 T. C. Holgate, *et al.*, Increasing the efficiency of the multi-mission radioisotope thermoelectric generator, *J. Electron. Mater.*, 2015, **44**, 1814–1821, DOI: **10.1007/s11664-014-3564-9**.

5 R. Gurunathan, R. Hanus and G. J. Snyder, Alloy scattering of phonons, *Mater. Horiz.*, 2020, **7**, 1452–1456, DOI: **10.1039/c9mh01990a**.

6 R. Gurunathan, R. Hanus, M. Dylla, A. Katre and G. J. Snyder, Analytical models of phonon-point-defect scattering, *Phys. Rev. Appl.*, 2020, **13**(3), 034011, DOI: **10.1103/PhysRevApplied.13.034011**.

7 L. Borgsmiller, D. Zavanelli and G. J. Snyder, Phase-boundary mapping to engineer defects in thermoelectric materials, *PRX Energy*, 2022, **1**, 022001, DOI: **10.1103/prxenergy.1.022001**.

8 C. Hu, K. Xia, C. Fu, X. Zhao and T. Zhu, Carrier grain boundary scattering in thermoelectric materials, *Energy Environ. Sci.*, 2022, **15**, 1406–1422, DOI: **10.1039/d1ee03802h**.

9 A. P. Justl, *et al.*, Unlocking the thermoelectric potential of the $Ca_{14}AlSb_{11}$ structure type, *Sci. Adv.*, 2022, **8**, 3780, DOI: **10.1126/sciadv.abq3780**.

10 M. Zhu, *et al.*, Defect modulation on $CaZn_{1-x}Ag_{1-y}Sb$ ($0 < x < 1$; $0 < y < 1$) Zintl phases and enhanced thermoelectric properties with high zT plateaus, *J. Mater. Chem. A*, 2018, **6**, 11773–11782, DOI: **10.1039/c8ta04001j**.

11 C. Fu, T. Zhu, Y. Liu, H. Xie and X. Zhao, Band engineering of high performance p-type FeNbSb based half-Heusler thermoelectric materials for figure of merit $zT > 1$, *Energy Environ. Sci.*, 2015, **8**, 216–220, DOI: **10.1039/c4ee03042g**.

12 S. Ohno, *et al.*, Achieving $zT > 1$ in Inexpensive Zintl Phase $Ca_9Zn_{4+x}Sb_9$ by Phase Boundary Mapping, *Adv. Funct. Mater.*, 2017, **27**, 1606361, DOI: **10.1002/adfm.201606361**.

13 S. R. Brown, S. M. Kauzlarich, F. Gascoin and G. J. Snyder, $Yb_{14}MnSb_{11}$: New high efficiency thermoelectric material for power generation, *Chem. Mater.*, 2006, **18**, 1873–1877, DOI: **10.1021/cm060261t**.

14 Y. Hu, J. Wang, A. Kawamura, K. Kovnir and S. M. Kauzlarich, $Yb_{14}MgSb_{11}$ and $Ca_{14}MgSb_{11}$-New Mg-containing Zintl compounds and their structures, bonding, and thermoelectric properties, *Chem. Mater.*, 2015, **27**, 343–351, DOI: **10.1021/cm504059t**.

15 A. He, *et al.*, Structural Complexity and High Thermoelectric Performance of the Zintl Phase: $Yb_{21}Mn_4Sb_{18}$, *Chem. Mater.*, 2019, **31**, 8076–8086, DOI: **10.1021/acs.chemmater.9b02671**.

16 S. Baranets, A. Ovchinnikov and S. Bobev, Complex Structural Disorder in the Zintl Phases $Yb_{10}MnSb_9$ and $Yb_{21}Mn_4Sb_{18}$, *Inorg. Chem.*, 2021, **60**, 6702–6711, DOI: **10.1021/ACS.INORGCHEM.1C00519**.

17 S. M. Kauzlarich, *Chemistry, Structure, and Bonding of Zintl Phases and Ions*, VCH Publishers, 1996.

18 S. M. Kauzlarich, S. R. Brown and G. J. Snyder, Zintl phases for thermoelectric devices, *J. Chem. Soc., Dalton Trans.*, 2007, 2099–2107, DOI: **10.1039/b702266b**.

19 E. S. Toberer, A. F. May and G. J. Snyder, Zintl chemistry for designing high efficiency thermoelectric materials, *Chem. Mater.*, 2010, **22**, 624–634, DOI: **10.1021/cm901956r**.

20 S. M. Kauzlarich, Zintl phases: From curiosities to impactful materials, *Chem. Mater.*, 2023, **35**, 7355–7362, DOI: **10.1021/acs.chemmater.3c01874**.

21 A. Jain, *et al.*, Commentary: the materials project: a materials genome approach to accelerating materials innovation, *APL Mater.*, 2013, **1**, 11002, DOI: **10.1063/1.4812323**.

22 J. E. Saal, S. Kirklin, M. Aykol, B. Meredig and C. Wolverton, Materials design and discovery with high-throughput density functional theory: the open quantum materials database (OQMD), *Jom*, 2013, **65**, 1501–1509, DOI: **10.1007/s11837-013-0755-4**.

23 S. Kirklin, *et al.*, The Open Quantum Materials Database (OQMD): Assessing the accuracy of DFT formation energies, *npj Comput. Mater.*, 2015, **1**, 15010, DOI: **10.1038/npjcompumats.2015.10**.

24 S. Q. Xia and S. Bobev, New manganese-bearing antimonides and bismuthides with complex structures. synthesis, structural characterization, and electronic properties of $Yb_9Mn_{4+x}Pn_9$ (Pn = Sb or Bi), *Chem. Mater.*, 2010, **22**, 840–850, DOI: **10.1021/cm901633r**.

25 Y. Y. Wang, S. Xu, L. L. Sun and T. L. Xia, Quantum oscillations and coherent interlayer transport in a new topological Dirac semimetal candidate $YbMnSb_2$, *Phys. Rev. Mater.*, 2018, **2**(2), 021201(R), DOI: **10.1103/PhysRevMaterials.2.021201**.

26 R. Rühl and W. Jeitschko, New pnictides with Ce_2O_2S-type structure, *Mater. Res. Bull.*, 1979, **14**, 513–517, DOI: **10.1016/0025-5408(79)90194-6**.

27 A. Kawamura, Y. Hu and S. M. Kauzlarich, Synthesis and Thermoelectric Properties of the YbTe–YbSb System, *J. Electron. Mater.*, 2016, **45**, 779–785, DOI: **10.1007/s11664-015-4202-x**.

28 H. Clark, H. Simpson and H. Steinfink, The crystal structure of $Yb_{11}Sb_{10}$, *Inorg. Chem.*, 1970, **9**(8), 1962–1964.

29 J. H. Grebenkemper, *et al.*, High temperature thermoelectric properties of $Yb_{14}MnSb_{11}$ prepared from reaction of MnSb with the elements, *Chem. Mater.*, 2015, **27**, 5791–5798, DOI: **10.1021/acs.chemmater.5b02446**.

30 S. R. Brown, S. M. Kauzlarich, F. Gascoin and G. J. Snyder, High-temperature thermoelectric studies of $A_{11}Sb_{10}$ (A = Yb, Ca), *J. Solid State Chem.*, 2007, **180**, 1414–1420, DOI: **10.1016/j.jssc.2007.02.007**.

31 K. P. Devlin, *et al.*, Enhancement of the Thermal Stability and Thermoelectric Properties of $Yb_{14}MnSb_{11}$ by Ce Substitution, *Chem. Mater.*, 2020, **32**, 9268–9276, DOI: **10.1021/acs.chemmater.0c03043**.

32 Y. Hu, *Zintl Phases with Complex Structure: Structure, Magnetism and Thermoelectric Properties of $A_{14}MPn_{11}$ Structure Type Compounds*, 2017.

33 L. Borgsmiller and G. J. Snyder, Thermoelectric properties and low thermal conductivity of Zintl compound $Yb_{10}MnSb_9$, *J. Mater. Chem. A*, 2022, **10**, 15127–15135, DOI: **10.1039/D2TA03114K**.

34 L. Borgsmiller, Q. Li, M. Y. Toriyama and G. J. Snyder, New Zintl Phase $Yb_{10}MgSb_9$ with High Thermoelectric Performance, *Adv. Energy Mater.*, 2023, 2300393, DOI: **10.1002/aenm.202300393**.

35 L. Borgsmiller, M. Y. Toriyama and G. J. Snyder, $Yb_{11}Sb_{10}$ and $Yb_{10}MnSb_9$ – Small Change in Structure Leads to Profound Differences in Thermoelectric Properties

Investigated Using Zintl Concepts, *Chem. Mater.*, 2024, **36**, 5542–5551, DOI: 10.1021/acs.chemmater.4c00486.

36 L. Borgsmiller, *et al.*, Anion Redox Balances Valence against Compositional Fluctuations in the 10-1-9 Zintl Family, *Chem. Mater.*, 2023, **35**, 10150–10155, DOI: 10.1021/acs.chemmater.3c02228.

37 A. P. Justl, G. Cerretti, S. K. Bux and S. M. Kauzlarich, 2 + 2 = 3: making ternary phases through a binary approach, *Chem. Mater.*, 2022, **34**, 1342–1355, DOI: 10.1021/acs.chemmater.1c04031.

38 A. P. Justl and S. M. Kauzlarich, Probing High-Temperature Oxidation of Thermoelectric Phases $Yb_{14}MSb_{11}$ (M = Mg, Mn, Zn), *ACS Appl. Mater. Interfaces*, 2022, **14**, 47246–47254, DOI: 10.1021/acsami.2c13093.

39 J. Y. Chan, M. M. Olmstead, S. M. Kauzlarich and D. J. Webb, Structure and Ferromagnetism of the Rare-Earth Zintl Compounds: $Yb_{14}MnSb_{11}$ and $Yb_{14}MnBi_{11}$, *Chem. Mater.*, 1998, **36**, 3583–3588.

40 A. Ovchinnikov, S. Chanakian, A. Zevalkink and S. Bobev, Ultralow Thermal Conductivity and High Thermopower in a New Family of Zintl Antimonides $Ca_{10}MSb_9$ (M = Ga, In, Mn, Zn) with Complex Structures and Heavy Disorder, *Chem. Mater.*, 2021, **33**, 3172–3186, DOI: 10.1021/acs.chemmater.0c04940.

41 H. M. Rietveld, A profile refinement method for nuclear and magnetic structures, *J. Appl. Crystallogr.*, 1969, **2**, 65–71, DOI: 10.1107/s0021889869006558.

42 J. B. Vaney, *et al.*, Effective medium theory based modeling of the thermoelectric properties of composites: comparison between predictions and experiments in the glass–crystal composite system $Si_{10}As_{15}Te_{75}$-$bi_{0.4}sb_{1.6}te_3$, *J. Mater. Chem. C*, 2015, **3**, 11090–11098, DOI: 10.1039/c5tc02087e.

43 M. Li, *et al.*, Unravelling Effective-Medium transport and interfacial resistance in $(CaTe)_x(GeTe)_{100-x}$ thermoelectrics, *Chem. Eng. J.*, 2023, **452**, 139269, DOI: 10.1016/j.cej.2022.139269.

44 Y. Wang, B. Qin and L. D. Zhao, Understanding the electrical transports of p-type polycrystalline SnSe with effective medium theory, *Appl. Phys. Lett.*, 2021, **119**, 044103, DOI: 10.1063/5.0058385.

45 T. W. Day, W. G. Zeier, D. R. Brown, B. C. Melot and G. J. Snyder, Determining conductivity and mobility values of individual components in multiphase composite $Cu_{1.97}Ag_{0.03}Se$, *Appl. Phys. Lett.*, 2014, **105**, 172103, DOI: 10.1063/1.4897435.

46 R. Landauer, The electrical resistance of binary metallic mixtures, *J. Appl. Phys.*, 1952, **23**, 779–784, DOI: 10.1063/1.1702301.

47 D. Stroud, Generalized effective-medium approach to the conductivity of an inhomogeneous materials, *Phys. Rev. B*, 1975, **12**, 3368–3373.

48 D. J. Bergman and O. Levy, Thermoelectric properties of a composite medium, *J. Appl. Phys.*, 1991, **70**, 6821–6833, DOI: 10.1063/1.349830.

49 J. Sonntag, Disordered electronic systems. iii. thermoelectric power in alloys with phase separation, *Phys. Rev. B*, 2006, **73**, 045126, DOI: 10.1103/PhysRevB.73.045126.

50 J. Sonntag, Thermoelectric power in alloys with phase separation (composites), *J. Phys.: Condens.Matter*, 2009, **21**, 175703, DOI: 10.1088/0953-8984/21/17/175703.

51 A. D. LaLonde, T. Ikeda and G. J. Snyder, Rapid consolidation of powdered materials by induction hot pressing, *Rev. Sci. Instrum.*, 2011, **82**, 1–4, DOI: 10.1063/1.3534080.

52 K. A. Borup, *et al.*, Measurement of the electrical resistivity and Hall coefficient at high temperatures, *Rev. Sci. Instrum.*, 2012, **83**, 123902, DOI: 10.1063/1.4770124.

53 S. Iwanaga, E. S. Toberer, A. Lalonde and G. J. Snyder, A high temperature apparatus for measurement of the Seebeck coefficient, *Rev. Sci. Instrum.*, 2011, **82**, 063905, DOI: 10.1063/1.3601358.

54 B. H. Toby and R. B. V. Dreele, GSAS-II: the genesis of a modern open-source all purpose crystallography software package, *J. Appl. Crystallogr.*, 2013, **46**, 544–549, DOI: 10.1107/S0021889813003531.